PERGAMON

International Journal of Solids and Structures 40 (2003) 4399–4416

INTERNATIONAL JOURNAL OF SOLIDS and STRUCTURES

www.elsevier.com/locate/ijsolstr

The influence of elastic constants on the shape of an inclusion

S. Kolling *, R. Mueller, D. Gross

Institute of Mechanics, TU Darmstadt, Hochschulstr.1, Darmstadt D-64289, Germany

Received 4 December 2002; received in revised form 25 March 2003

Abstract

A continuum mechanics model is proposed to investigate coherent misfitting precipitates in a matrix material. This elasticity based method takes arbitrary anisotropic materials, eigenstrains and interface energies into account. The equilibrium shape of the precipitate is described in terms of Eshelby's driving forces acting on the precipitate interface. According to this force, an efficient shape optimization technique is formulated to investigate the influence of various parameters such as particle size, elastic constants and inhomogeneity on the equilibrium morphology. Using stable equilibrium shapes, the macroscopical response of the composite is calculated and compared with some common approximation techniques. The numerical treatment is realised with the finite element method.

Keywords: Microstructure; Configurational forces; Inhomogeneity; Finite elements

1. Introduction

The prediction of material properties of heterogeneous materials presents a difficulty if the microstructure changes during mechanical or thermal influence. This happens for example in single-crystal Ni-base superalloys used in many modern high temperature applications, where the microstructure is formed by coherent precipitates (γ'-phase) in a matrix material (γ-phase). To understand the material behaviour and the temporal evolution of the precipitate shape in detail, a lot of experimental, theoretical and numerical work has been done in the last few years. While purely analytical formulations are very restricted to simple cases, a generalized treatment of the problem can only be achieved by computational investigations, where the numerical models are either of stochastic or deterministic nature.

One possibility to simulate equilibrium morphologies is to use the Monte Carlo type atomistic simulations (Binder, 1986) based on a combination of statistical mechanics and linear elasticity. The first- and simplest-stochastic model for spinodal decomposition and diffusive growth of particles from a supersaturated matrix is the Ising-model from 1924. Actually developed to describe magnetizing, the model is recently applied to questions associated with binary mixtures, see (Glotzer et al., 1994). Such a simple model is, however, unable to consider the elastic interaction of particles. This has been achieved by the

* Corresponding author. Tel.: +49-6151-162980; fax: +49-6151-163018.
E-mail address: kolling@mechanik.tu-darmstadt.de (S. Kolling).

0020-7683/03/$ - see front matter © 2003 Elsevier Ltd. All rights reserved.
doi:10.1016/S0020-7683(03)00183-5

discrete atom method (DAM) (see Lee, 1995). Within the DAM-model, the material is represented by an elastic triangular lattice considering the nearest neighbours. Because of the chosen lattice structure, the model is restricted to a Poisson ratio of 0.25 in the isotropic case (Lee, 1996). A continuum generalization called Gauss point method (GPM) was capable to overcome the restriction of the DAM (see Kolling and Gross, 2001). Considering the Gauss integration point within a finite element as a lattice place, arbitrary material parameters can be used. All these models are very time consuming for computing the equilibrium shapes of the precipitates. If parameter investigations are required, deterministic models are favorable. Here, mainly two different approaches using a sharp or a diffusive interface are worth mentioning.

In sharp interface models, the γ- and the γ'-phase are separated by a singular surface and a generalized thermodynamic force acting on the interface is introduced (Thompson et al., 1994; Socrate and Parks, 1993). The equilibrium shape of the inhomogeneity is found by minimization of the total potential. A generalization of this theory has been done by extending the simulations to inhomogeneous settings (Schmidt and Gross, 1995), fully 3D-case (Mueller and Gross, 1998) and interaction with other material defects like microcracks (Kolling et al., 2002).

Another useful tool is the continuous description of the interface via equations of the Cahn–Hilliard type (Cahn and Hilliard, 1958) developed in order to describe spinodal decomposition at early stages of the process and, subsequently, diffusive growth of particles in a supersaturated matrix at later stages (Küpper and Masbaum, 1994). This nonlinear diffusion equation originally contained no elastic strain energy. This has been achieved in a special form recently (e.g. see Dreyer and Müller, 2000).

The intent of this paper is, on the one hand, to show the influence of elastic constants on the stability of an inhomogeneity with misfitting eigenstrains following (Schmidt and Gross, 1997). On the other hand, the influence of the macroscopical response of the material behaviour during the temporal evolution of the morphology will be discussed.

In Section 2 the basic equations for the sharp interface model, the total energy and the driving force acting on the interface will be derived. Furthermore, some homogenization approximations for the global material behaviour are discussed. In Section 3 the numerical methods for calculating the driving forces via finite elements and a shape optimization technique are described in detail. A discussion and a summary of the results are presented in Sections 4 and 5.

2. Micromechanical model

Considered is a misfitting isolated precipitate $\mathscr{B}_I$ with elasticity tensor $\mathbb{C}_I$ and lattice constant $a_{\gamma'}$ in a finite matrix domain $\mathscr{B}_M$ with elasticity tensor $\mathbb{C}_M$ and lattice constant a_γ. Thus, the γ'-phase is modeled by an eigenstrain $\boldsymbol{\varepsilon}^0 = (a_{\gamma'} - a_\gamma)/a_\gamma \mathbf{1}$ in $\mathscr{B}_I$ caused by the difference in the lattice constants. The two regions are separated by a sharp interface $\partial\mathscr{B}$ (see Fig. 1).

2.1. Configurational forces

In the aforementioned model, the free energy ψ of the system depends on the strain $\boldsymbol{\varepsilon} = \frac{1}{2}(\nabla\mathbf{u} + (\nabla\mathbf{u})^{\mathrm{T}})$, where $\boldsymbol{u}$ is the displacement. And because of the interface, ψ depends explicitly on the position $\boldsymbol{x}$: $\psi = \hat{\psi}(\boldsymbol{\varepsilon}; \boldsymbol{x})$. Now, we investigate the energy change of the system by computing the gradient

$$\nabla\psi = \underbrace{\frac{\partial\hat{\psi}}{\partial\boldsymbol{\varepsilon}}}_{=\boldsymbol{\sigma}} : \nabla\nabla\boldsymbol{u} + \left.\frac{\partial\hat{\psi}}{\partial\boldsymbol{x}}\right|_{\text{expl.}}, \tag{1}$$

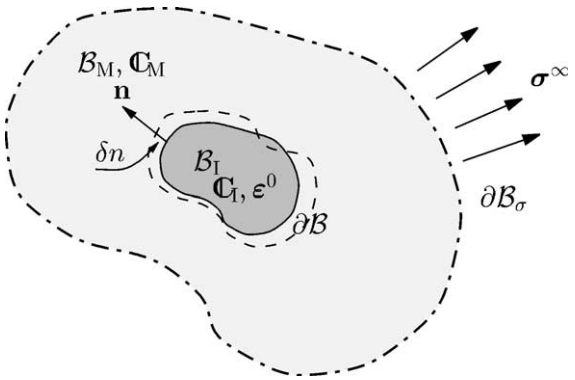

Fig. 1. Continuum mechanical model.

where $\boldsymbol{\sigma} : \nabla\nabla\boldsymbol{u}$ is $\sigma_{ij}u_{i,jk}$ in index notation for Cartesian coordinates. Rewriting (1) and using the mechanical equilibrium condition $\operatorname{div}\boldsymbol{\sigma} + \boldsymbol{f} = \mathbf{0}$ we get

$$\left.\frac{\partial\hat{\psi}}{\partial\boldsymbol{x}}\right|_{\text{expl.}} = \nabla\psi - \operatorname{div}(\nabla\boldsymbol{u}^{\mathrm{T}}\boldsymbol{\sigma}) + \nabla\boldsymbol{u}^{\mathrm{T}}\underbrace{\operatorname{div}\boldsymbol{\sigma}}_{=-\boldsymbol{f}} = \operatorname{div}(\psi\mathbf{1} - (\nabla\boldsymbol{u})^{\mathrm{T}}\boldsymbol{\sigma}) - \nabla\boldsymbol{u}^{\mathrm{T}}\boldsymbol{f} \tag{2}$$

and achieve a balance equation of the form

$$\operatorname{div}(\underbrace{\psi\mathbf{1} - (\nabla\boldsymbol{u})^{\mathrm{T}}\boldsymbol{\sigma}}_{:=\boldsymbol{\Sigma}}) - \underbrace{\nabla\boldsymbol{u}^{\mathrm{T}}\boldsymbol{f} - \left.\frac{\partial\hat{\psi}}{\partial\boldsymbol{x}}\right|_{\text{expl.}}}_{:=\mathbf{g}} = \mathbf{0}. \tag{3}$$

Here, $\boldsymbol{\Sigma}$ is the energy-momentum tensor (Eshelby, 1951, 1970) and the term $\mathbf{g}$ is called configurational (body) force. In some literature, Eshelby-stress tensor and material force are other names for $\boldsymbol{\Sigma}$ and $\mathbf{g}$. Note that (3) has the same structure as the mechanical equilibrium condition.

2.2. Force on the inclusion

In absence of body forces, the total potential Π of the model can be written as a sum of elastic strain energy Π_{el}, the potential of the external loads Π_{ext} and the interfacial energy Π_{int}.

The mechanical part is given by

$$\Pi_{\text{el}} + \Pi_{\text{ext}} = \frac{1}{2}\int_{\mathcal{B}_I}(\boldsymbol{\varepsilon} - \boldsymbol{\varepsilon}^0) : [\mathbb{C}_I(\boldsymbol{\varepsilon} - \boldsymbol{\varepsilon}^0)]\,\mathrm{d}V + \frac{1}{2}\int_{\mathcal{B}_M}\boldsymbol{\varepsilon} : [\mathbb{C}_M\boldsymbol{\varepsilon}]\,\mathrm{d}V - \int_{\partial\mathcal{B}_M}\hat{\mathbf{t}}\cdot\mathbf{u}\,\mathrm{d}A, \tag{4}$$

were $\hat{\mathbf{t}} = \boldsymbol{\sigma}^\infty\boldsymbol{n}$ is the external load. The displacement is continuous for a coherent interface:

$$[\![\boldsymbol{u}]\!] = \mathbf{0}, \quad \forall\boldsymbol{x} \in \partial\mathcal{B}. \tag{5}$$

The operator $[\![(\cdot)]\!]$ denotes the jump between outer and inner limit of a quantity across the interface $\partial\mathcal{B}$. The interfacial part Π_{int} of the total energy is given by

$$\Pi_{\text{int}} = \int_{\partial\mathcal{B}}\gamma\,\mathrm{d}A, \tag{6}$$

where γ is an isotropic interfacial energy density. In general γ can be anisotropic, but for simplicity we restrict attention to the isotropic case in this paper.

2.3. Equilibrium shape

In general, morphologies, which extremize the total potential Π are named equilibrium shapes. A necessary condition for a morphology to be an equilibrium shape is that the first variation of Π vanishes ($\delta\Pi = 0$). Restricting the volume of the inclusion V_I to remain constant (mass conservation: $V_I = V_0$) during the variation, the equilibrium shape can be analyzed at various prescribed particle sizes. To fulfill the constrained, the potential Π is augmented by a Lagrange multiplier λ:

$$\mathscr{L} = \Pi + \Pi_\lambda = \Pi + \lambda(V_I - V_0). \tag{7}$$

The variation of this Lagrange functional (see Mueller et al., 2000 for details) results in

$$\delta\mathscr{L} = -\int_{\partial\mathscr{B}} (\mathsf{G}_\mathrm{n} - \lambda)\delta n \,\mathrm{d}A + \delta\lambda(V_I - V_0), \tag{8}$$

where δn denotes a shape variation of the interface along its normal and

$$\mathsf{G}_\mathrm{n} = \underbrace{\mathbf{n}\cdot[\![\boldsymbol{\Sigma}]\!]\mathbf{n}}_{\mathsf{G}_\mathrm{n}^\mathrm{el}} + \underbrace{\gamma\kappa}_{\mathsf{G}_\mathrm{n}^\mathrm{int}} \tag{9}$$

represents the configurational force. It consists of an elastic part $\mathsf{G}_\mathrm{n}^\mathrm{el}$, which can be expressed by an explicit formula as well (see Schmidt and Gross, 1999) and an interface part $\mathsf{G}_\mathrm{n}^\mathrm{int}$. Furthermore, $\mathbf{n}$ is the outward unit normal vector on $\partial\mathscr{B}$, κ is twice the mean curvature of the interface and $\boldsymbol{\Sigma}$ is Eshelby's energy momentum tensor from (3). Since $\delta\mathscr{L}$ has to be zero at a stationary point, a necessary condition for arbitrary variations δn and $\delta\lambda$ is that both brackets in Eq. (8) have to be zero, ergo G_n has to be constant on $\partial\mathscr{B}$. Thus, we define the mean value of G_n as

$$\langle\mathsf{G}_\mathrm{n}\rangle := \frac{\int_{\partial\mathscr{B}} \mathsf{G}_\mathrm{n}\mathrm{d}A}{\int_{\partial\mathscr{B}} \mathrm{d}A} = \text{const.} \tag{10}$$

For any deviation from this average value, the driving force either acts as a pressure or as a traction on the interface (according to its sign) towards an equilibrium shape. For an equilibrium shape, (10) corresponds the Lagrange multiplier: $\langle\mathsf{G}_\mathrm{n}\rangle \equiv \lambda$.

2.4. Macroscopical response

For the overall properties of the material with inhomogeneities in equilibrium morphology, we use the standard representative volume element (RVE) technique. Here, we consider the matrix boundary ∂V surrounding the entire volume $V = V_I \cup V_M$ as a RVE. The average values of the stress and strain fields are given by

$$\langle\boldsymbol{\sigma}\rangle = \frac{1}{V}\int_V \boldsymbol{\sigma}(\boldsymbol{x})\,\mathrm{d}V = \frac{1}{V}\int_{\partial V} \boldsymbol{t}\otimes\boldsymbol{x}\,\mathrm{d}A \tag{11}$$

and

$$\langle\boldsymbol{\varepsilon}\rangle = \frac{1}{V}\int_V \boldsymbol{\varepsilon}(\boldsymbol{x})\,\mathrm{d}V = \frac{1}{2V}\int_{\partial V} (\boldsymbol{u}\otimes\boldsymbol{n} + \boldsymbol{n}\otimes\boldsymbol{u})\,\mathrm{d}A. \tag{12}$$

The operator $\langle(\cdot)\rangle$ denotes the average value of a quantity $(\cdot)$ in V. The effective (macroscopic observable) stiffness tensor $\mathbb{C}^\mathrm{eff}$ can easily be computed by using three (2D) or six (3D) linear independent stress ($\boldsymbol{\varepsilon}|_{\partial V} = \boldsymbol{\varepsilon}^\infty = \langle\boldsymbol{\varepsilon}\rangle$) or strain ($\boldsymbol{\sigma}|_{\partial V} = \boldsymbol{\sigma}^\infty = \langle\boldsymbol{\sigma}\rangle$) boundary conditions:

$$\langle\boldsymbol{\sigma}\rangle = \mathbb{C}^\mathrm{eff} : \langle\boldsymbol{\varepsilon}\rangle. \tag{13}$$

However, it must be noted that, of course, it exists a macroscopical eigenstrain due to the eigenstrain $\boldsymbol{\varepsilon}^0$ of the inhomogeneity. But in this investigation, we are only interested in the effective stiffness of the material, which is independent of an existing $\boldsymbol{\varepsilon}^0$.

Some of the most common estimations of the effective material properties are shortly outlined in what follows, for details see the books by Mura (1987) and Nemat-Nasser and Hori (1993). The simplest approximations are according to Voigt $\mathbb{C}_{\mathrm{V}}^{\mathrm{eff}}$ assuming constant strain in V and Reuss $\mathbb{C}_{\mathrm{R}}^{\mathrm{eff}}$ assuming constant stress in V:

$$\mathbb{C}_{\mathrm{V}}^{\mathrm{eff}} = c_I\mathbb{C}_I + c_M\mathbb{C}_M, \qquad \mathbb{C}_{\mathrm{R}}^{\mathrm{eff}} = (c_I\mathbb{C}_I^{-1} + c_M\mathbb{C}_M^{-1})^{-1}. \tag{14}$$

Here, $c_i = V_i/V$ is the corresponding volume fracture of the considered phase $i = I, M$. In an energy manner, $\mathbb{C}_{\mathrm{V}}^{\mathrm{eff}}$ is an upper bound and $\mathbb{C}_{\mathrm{R}}^{\mathrm{eff}}$ is a lower bound for effective stiffness approximations. Further analytical approximations can easily be achieved if ellipsoidal inclusions are considered together with isotropic matrix materials. By using the average strain assumption $\boldsymbol{\varepsilon}^\infty = \langle\boldsymbol{\varepsilon}\rangle$, the so-called dilute distribution method yields

$$\mathbb{C}_{\mathrm{DD}}^{\mathrm{eff}} = \mathbb{C}_M + c_I[\![\mathbb{C}]\!] : [\mathbb{1} + \mathbb{P}_M : \mathbb{C}_M^{-1} : [\![\mathbb{C}]\!]]^{-1}. \tag{15}$$

Here, $\mathbb{P}_M$ is Eshelby's tensor of the isotropic matrix phase, which depends also on the aspect ratio of the ellipse. As the main assumption of this method, the interaction between inhomogeneities is neglected, ergo the matrix phase dominates: $c_I \ll c_M$. Mori and Tanaka gave an approximation which is capable to consider higher volume fraction with interacting particles by assuming the equivalence of the macroscopic and matrix strain ($\boldsymbol{\varepsilon}^\infty = \langle\boldsymbol{\varepsilon}\rangle_M$) or stress ($\boldsymbol{\sigma}|_{\partial V} = \langle\boldsymbol{\sigma}\rangle_M$):

$$\mathbb{C}_{\mathrm{MT}}^{\mathrm{eff}} = \mathbb{C}_M + c_I[\![\mathbb{C}]\!] : [\mathbb{1} + c_M\mathbb{P}_M : \mathbb{C}_M^{-1} : [\![\mathbb{C}]\!]]^{-1}. \tag{16}$$

3. Numerical methods

3.1. Field equations

For the numerical treatment of the driving forces (9) the required field equations in (3) are calculated via standard finite elements. An iso-parametrical formulation of an element Ω_e leads to the global residual

$$\cup_{e=1}^{n_{\mathrm{el}}} \sum_{J=1}^{N} \boldsymbol{\eta}^J \cdot \left[\sum_{K=1}^{N} \int_{\Omega_e} \boldsymbol{B}_J^{\mathrm{T}}\boldsymbol{\sigma}_K \,\mathrm{d}\Omega - \int_{\partial\Omega_e^\sigma} N_J\hat{\boldsymbol{t}}\,\mathrm{d}\Gamma \right] = \mathbf{0}. \tag{17}$$

Here, N are the number of nodes per element, $\boldsymbol{\eta}$ is a test function, the matrix $\boldsymbol{B}_J$ contains the derivatives of the shape functions N_J, $\hat{\boldsymbol{t}} = \boldsymbol{\sigma}^\infty\boldsymbol{n}$ denotes an external load vector acting on the element boundary $\partial\Omega_e^\sigma$ and the operator $\cup$ denotes the required assemblage of all elements. If this system of equations is solved, the energy momentum tensor $\boldsymbol{\Sigma}$ in (3) and the average values (11) and (12) can be computed easily in a post processing.

3.2. Configurational forces

Starting point for calculating G_{n} is the weak formulation of (3)

$$\int_{\mathscr{B}} (\operatorname{div}\boldsymbol{\Sigma} + \mathbf{g}) \cdot \boldsymbol{\eta}\,\mathrm{d}V = \int_{\mathscr{B}} (-\boldsymbol{\Sigma} : \nabla\boldsymbol{\eta} + \mathbf{g}\cdot\boldsymbol{\eta})\,\mathrm{d}V + \int_{\partial\mathscr{B}} \boldsymbol{\Sigma}\boldsymbol{n}\cdot\boldsymbol{\eta}\,\mathrm{d}A = 0, \tag{18}$$

where $\boldsymbol{\eta}$ is again a test function, but has not to be the same as in (17) necessarily. If we assume stationary boundaries, the test function $\boldsymbol{\eta}$ is zero on $\partial\mathscr{B}$ and the boundary integral in (18) vanishes. In a post processing, we compute $\boldsymbol{\Sigma}$ in every Gauss-point of the element and obtain the driving force acting on the node J by

$$\mathbf{G}^J = \cup_{\mathrm{e}=1}^{n_{\mathrm{el}}^*} \int_{\Omega_\mathrm{e}} \boldsymbol{\Sigma}\nabla N^J \,\mathrm{d}\Omega. \tag{19}$$

Now, the operator $\cup$ denotes the assemblage of all n_{el}^* elements adjacent to node J. For further details and applications of this computational technique for a wide range of material science, see (Mueller et al., 2002; Steinmann, 2000; Steinmann et al., 2001). The relation between $\mathbf{G}^J$ in (19) and G_n in (9) is outlined in Appendix A.

3.3. Shape optimization

The equilibrium shape of the inhomogeneity is obtained by extremizing the augmented Lagrangian $\mathscr{L}$ with respect to the surface $\partial\mathscr{B}$ of the precipitate. Therefore, the considered surface of the inhomogeneity is described by a set of M shape parameters q_i. Then, the variation in normal direction is given by

$$\delta n = \frac{\partial \mathbf{x}}{\partial q_i} \cdot \mathbf{n}\delta q_i \quad \forall \mathbf{x} \in \partial\mathscr{B}, \quad i = 1, \ldots, M. \tag{20}$$

Inserting (20) in the augmented potential (8) leads to a system of $M+1$ nonlinear equations

$$\begin{aligned}
F_1(q_i,\lambda) &= -\int_{\partial\mathscr{B}} (\mathsf{G}_\mathrm{n} - \lambda)\frac{\partial \mathbf{x}}{\partial q_1}\cdot\mathbf{n}\,\mathrm{d}A = 0,\\
&\vdots \qquad\qquad \vdots\\
F_M(q_i,\lambda) &= -\int_{\partial\mathscr{B}} (\mathsf{G}_\mathrm{n} - \lambda)\frac{\partial \mathbf{x}}{\partial q_M}\cdot\mathbf{n}\,\mathrm{d}A = 0,\\
F_{M+1}(q_i,\lambda) &= V_I - V_0 = 0,
\end{aligned}$$

which can be solved by quasi-Newton methods. Useful shape parameters are for example the radii $q_i = r_i$ of the interface nodes: $\boldsymbol{x}_i = \boldsymbol{e}_i^r r_i$, where $\boldsymbol{e}_i^r$ are the direction position vectors. Thus, the partial derivative in (20) remains $\partial \boldsymbol{x}_i/\partial r_i = \boldsymbol{e}_i^r$. Using quasi-Newton methods, this shape optimization is very efficient. However, it is not suitable to describe the temporal evolution of an initial shape towards an equilibrium one. For such kinetic investigations (see Mueller and Gross, 1999; Kolling and Gross, 2001; Kolling et al., 2003).

Using solely the aspect ratio $q := \rho = a/b$ of the principal axis a and b of the inhomogeneity as the most important shape parameter, the total potential depends on two parameters only: $\Pi = \Pi(\rho,\gamma)$. Because Π is a linear function in the interfacial energy γ, a critical value γ_{crit} due to Π can be approximated by calculating Π for two different values γ_0, γ_1 ($\gamma_0 < \gamma_1$) and elongations $\rho = 1$, $\rho = 1 + \Delta\rho$ ($\Delta\rho > 0$):

$$\gamma_{\mathrm{crit}} \approx \gamma_0 - \alpha_0(\gamma_1 - \gamma_0), \tag{21}$$

where

$$\alpha_0 = \left[\left.\frac{\mathrm{d}\Pi}{\mathrm{d}\rho}\right|_{\rho=1+\Delta\rho,\gamma_1} - \left.\frac{\mathrm{d}\Pi}{\mathrm{d}\rho}\right|_{\rho=1+\Delta\rho,\gamma_0}\right]^{-1} \left.\frac{\mathrm{d}\Pi}{\mathrm{d}\rho}\right|_{\rho=1+\Delta\rho,\gamma_0}. \tag{22}$$

It describes the transition from concave to convex curvature of the function along a fixed line $\rho = \mathrm{const}$. If no transition exists, γ_{crit} is identically zero. The physical meaning of this critical value will be discussed in detail below.

The stability of equilibrium configurations ρ_{equ} at $\gamma = \text{const.}$ are found by determining the minimum or maximum values of $\Pi(\rho, \gamma)$ respectively:

$$\left.\frac{\mathrm{d}^2\Pi}{\mathrm{d}\rho^2}\right|_{\rho=\rho_{\text{equ}}} \begin{cases} > 0 \rightarrow \text{stable}, \\ = 0 \rightarrow \text{critical point}, \\ < 0 \rightarrow \text{unstable}. \end{cases} \tag{23}$$

The second derivatives of the potential with respect to the aspect ratio are approximated by

$$\left.\frac{\mathrm{d}^2\Pi}{\mathrm{d}\rho^2}\right|_{\rho=\rho_{\text{equ}}} \approx \frac{\Pi(\rho_{\text{equ}} + \Delta\rho) - 2\Pi(\rho_{\text{equ}}) + \Pi(\rho_{\text{equ}} - \Delta\rho)}{\Delta\rho^2}. \tag{24}$$

4. Results

The following results are calculated in 2D under plane strain condition and no external loads are considered.

For a systematic investigation of the problem, it is useful to introduce the following dimensionless parameters:

$$L = \frac{\bar{l}\bar{\mu}_M\bar{\varepsilon}^2}{\gamma}, \quad \bar{\mathsf{G}}_{\text{n}} = \frac{\mathsf{G}_{\text{n}}}{\bar{l}\bar{\mu}_M(\bar{\varepsilon})^2}, \quad A = \frac{2C_{44}}{C_{11} - C_{12}}, \quad \mu^* = \frac{\bar{\mu}_I}{\bar{\mu}_M}. \tag{25}$$

Here $\bar{l} = \sqrt{\mathrm{A}_I}$ is a characteristic particle size, $\bar{\mu}_M$ the effective shear modulus defined in (26), which describes an average stiffness of the matrix material and $\bar{\varepsilon}$ is defined as the largest eigenvalue of the eigenstrain tensor $\boldsymbol{\varepsilon}^0$. Thus, the dimensionless particle size L is the ratio of a characteristic elastic energy to a characteristic interfacial energy. To obtain a critical particle size L_{crit}, set $\gamma \rightarrow \gamma_{\text{crit}}$ according to Eq. (21). Using the Voigt-notation of the fourth order stiffness tensor $\mathbb{C}$, a measure for the anisotropy of the materials is given by the ratio $A_I = A_M =: A$. The influence of $A_I \neq A_M$ has been already discussed in (Schmidt and Gross, 1997). But especially with respect to alloys, the anisotropic equality of the two phases presents a realistic assumption. The stiffness ratio μ^* is defined by the averaged shear modulus of the inclusion and the matrix. In an anisotropic material, the averaged Lamé-constants $\bar{\mu}$, $\bar{\lambda}$ and the averaged Poisson's ratio $\bar{\nu}$ are given by:

$$\bar{\mu} = \frac{1}{2\pi}\int_0^{2\pi} C_{1212}(\varphi)\,\mathrm{d}\varphi, \quad \bar{\lambda} = \frac{1}{2\pi}\int_0^{2\pi} C_{1122}(\varphi)\,\mathrm{d}\varphi, \quad \bar{\nu} = \frac{\bar{\lambda}}{2(\bar{\lambda} + \bar{\mu})}. \tag{26}$$

Here, the averaging has to be done over all orientations φ. With this choice we investigate the equilibrium morphology with respect to the parameter set $\mathscr{S} = \{L, \mu^*, A, \bar{\nu}_I, \bar{\nu}_M\}$ and, additionally, the macroscopic response with respect to the volume fraction c_I of the inclusion.

4.1. Equilibrium morphology

Due to the aspect ratio of the precipitate, the elastic strain energy defined in (4) is either a convex or a concave function depending on the stiffness ratio μ^* and has either a global minimum or a global maximum at $\rho^* := (\rho - 1/\rho + 1) = 0$. Contrary, the interfacial energy part is always convex, i.e. independent of μ^*, and has a global minimum at $\rho^*_{\text{equ}} = 0$. In combination, the convexity depends on the particle size L. Therefore, it exists a critical value L_{crit}, which has the meaning of a bifurcation point from convexity to concavity at $\rho^*_{\text{equ}} = 0$. This is true for fourfold symmetric convex precipitates, where the aspect ratio is well defined and if dilatational eigenstrains and orthotropic materials are considered. Under this conditions, we will discuss the main influence of the parameter set $\mathscr{S}$ on this bifurcation point in the following.

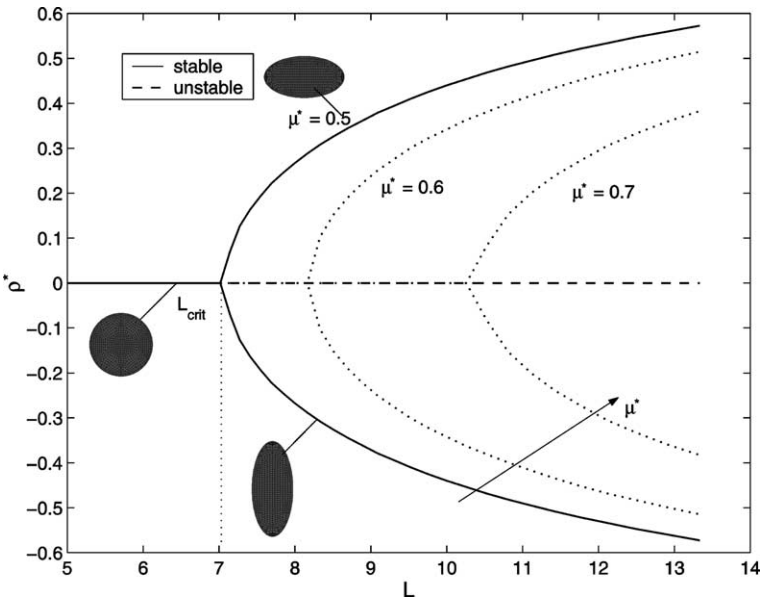

Fig. 2. Bifurcation diagram—influence of the stiffness ratio μ^* ($A = 1.0$).

For isotropic particles in an isotropic matrix ($A = 1.0$), the presented shape optimization leads to circular equilibrium shapes below the bifurcation point and elliptical shapes above of it. As it is shown in the stability diagram (see Fig. 2): if L is small enough, the minimum of the total potential is always given by a circle $\rho^*_{\text{equ}} = 0 \ \forall L \leqslant L_{\text{crit}}$. For over-critical values, the stable equilibrium shape (bifurcated solid line) is getting elliptical $\rho^*_{\text{equ}} \neq 0 \ \forall L > L_{\text{crit}}$, i.e. elongated in different principal directions for $\rho^*_{\text{equ}} < 0$ and $\rho^*_{\text{equ}} > 0$ respectively. At the same particle size, the circular shape presents an unstable equilibrium (dashed line). The solid line is calculated under the condition of $\lambda = \mu$ and $\mu^* = 0.5$. This should serve as a reference due to the other parameters. As can be seen, the bifurcation point strongly depends on the stiffness ratio. An increase of μ^* results in a shifting of the bifurcation curve up to higher values of L. However, the qualitative behaviour remains the same.

This can be explained by the curvature of Π in Fig. 3, where $\mathrm{d}^2\Pi/\mathrm{d}\rho^2$ at $\rho^*_{\text{equ}} = 0$ is drawn for different particle sizes. For the small value $L = 4$, $\Pi(\mu^*)$ is convex for all μ^*. Thus, there exist only circular equilibrium shapes: $\rho^*_{\text{equ}} = 0 \ \forall \mu^*$. For the larger particle $L = 10$, we obtain a change in the sign of the curvature for a certain range 0.2–0.7 of μ^*. This leads to elliptical shapes $\rho^{\text{equ}} \neq 0$ for all materials with $\mu^* = 0.2$–0.7 and circular shapes for other values of μ^*. This range gets more and more significant for increasing particle sizes. For $L \to \infty$, where the elastic energy dominates, only elliptical equilibrium shapes exist for soft particles ($\mu^* < \mu^*_{\text{as}} = 1.0$). For stiffer inclusions, only circular shapes are in equilibrium and there is no bifurcation point. Here, the asymptote μ^*_{as} defines the names of "soft" ($\mu^* < \mu^*_{\text{as}}$), "hard" ($\mu^* > \mu^*_{\text{as}}$) and "homogeneous" ($\mu^* = \mu^*_{\text{as}}$) inclusions.

However, even a decrease in the stiffness ratio leads to the aforementioned shifting of L_{crit}. Fig. 4 shows the bifurcation point as a function of the stiffness ratio μ^*. It also demonstrates the influence of inhomogeneity.

In the reference curve ($\lambda = \mu$) and for a stiffness ratio $\mu^* = 0.5$, the instability is reached at the critical particle size of $L_{\text{crit}} = 7.0$ (likewise depicted as a dotted line in Fig. 2). It exists both circular shapes and elongated shapes. For the transition to hard inclusions ($\mu^* \to \mu^*_{\text{as}}$) or very soft inclusions ($\mu^* \to 0$), only circles are possible and it exists no significant bifurcation point. However, for the smaller value $\mu^* = 0.32$,

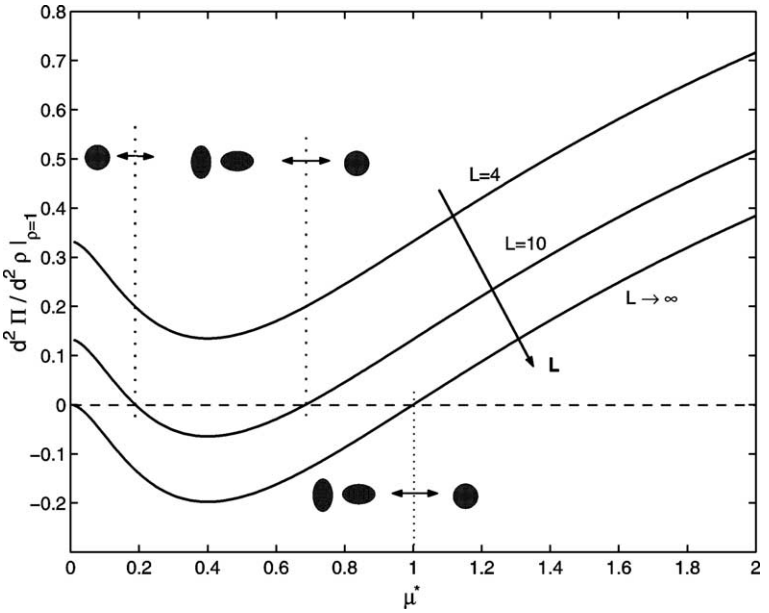

Fig. 3. Curvature for different particle sizes L ($A = 1.0$).

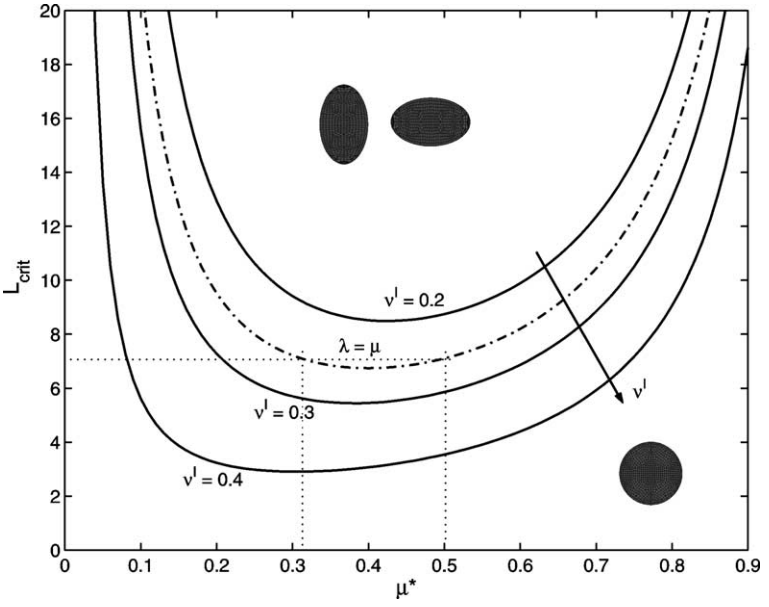

Fig. 4. Stiffness ratio and Poisson's ratio of the inclusion.

the instability is also reached at the same point. Therefore, a simple statement whether an increase of μ^* also increases the stability is not possible. It is only valid for a certain range of μ^*. In this case for roughly $\mu^* > 0.4$, the minimum of the curve.

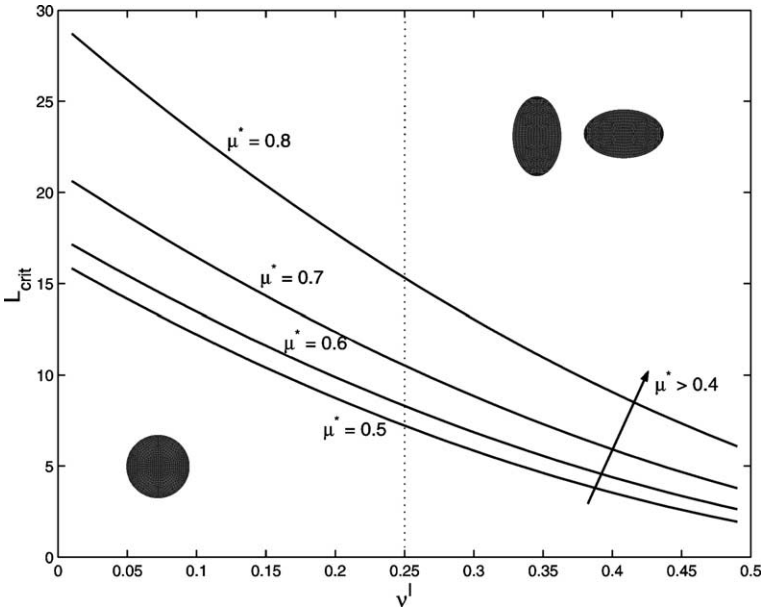

Fig. 5. Influence of Poisson's ratio ν_I for $\mu^* > 0.4$.

Likewise depicted in this figure is a variation of the inclusion's Poisson ratio ν_I. For smaller values of ν_I, the zone of stable circular equilibrium shapes becomes more and more dominant. This indicates a smaller Poisson's ratio as a stabilizing parameter for equilibrium shapes.

Fig. 5 shows this influence in detail. L_{crit} in dependence of ν_I is a monotonous decreasing function. The sensitivity for a stiffness ratio of $\mu^* > 0.4$ shows likewise a distinct stabilizing tendency. Contrary, for smaller values of μ^*, the stability additionally depends on the value of ν_I (see Fig. 6). As a reference serves the two stiffness ratios $\mu^* = 0.32$ and $\mu^* = 0.5$ (dotted lines in Fig. 4). For a Poisson's ratio of $\nu_I > 0.25$, an increase of the stiffness ratio also increases the stability. For $\nu_I < 0.25$, the stability decreases. Further investigations have shown that the effect of the Poisson ratio of the matrix ν_M on the stability can be neglected.

In order to describe the material behaviour of e.g. Ni-base superalloys, the isotropy has to be replaced by a realistic fcc/bcc crystal structure, which implies orthotropic symmetry. Considering this case, we have to pay attention to further phenomenons due to our set of parameters. For such a cubic material, the effective Lamé constants in Eq. (26) can be written as

$$\bar{\mu} = \tfrac{1}{4}[C_{11} - C_{12} + 2C_{44}], \qquad \bar{\lambda} = \tfrac{1}{4}[C_{11} + 3C_{12} - 2C_{44}]. \tag{27}$$

For orthotropic particles in an orthotropic matrix ($A > 1.0$), the presented shape optimization leads to cube-like equilibrium shapes. Like in the isotropic case the stable shapes are elongated above a certain bifurcation point.

As a reference material in the anisotropic case, we take $A = 2.5$, $\nu_I = \nu_M = 0.3$ and $\mu^* = 1.0$. It mimics, for example, the behaviour of nickel (dotted lines in Figs. 9 and 10). But in contrast to isotropic materials, bifurcation occurs even for a homogeneous particle ($\mu^* = 1.0$).

This stability behaviour is depicted in Fig. 7 by means of the curvature of the potential at $\rho^*_{\text{equ}} = 0$. Like in the isotropic case, $\Pi(\mu^*)$ is strictly convex for the small value $L = 4$ and only cubic shapes ($\rho^*_{\text{equ}} = 0$) exist. But for $L = 10$, we obtain a change in the sign of the curvature for a larger range of μ^* than for $A = 1$. This leads again to elongated equilibrium shapes for all stiffness ratios within this range and otherwise cubic

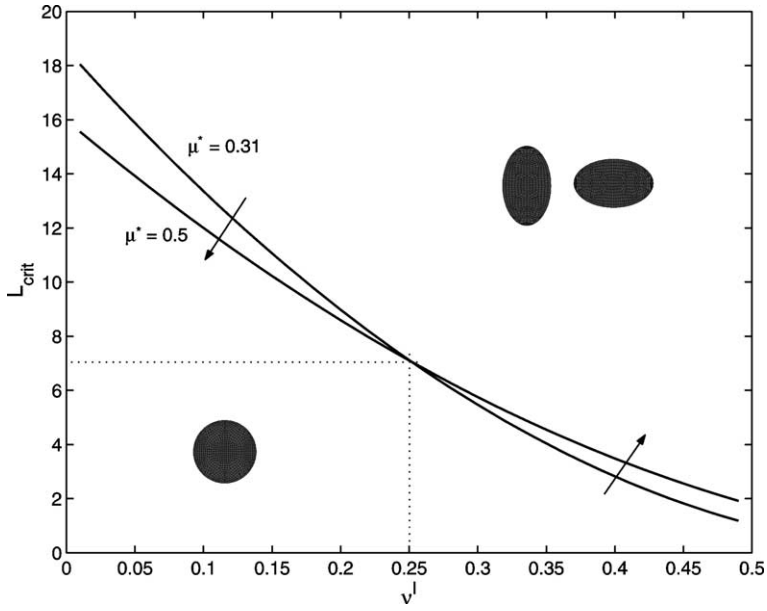

Fig. 6. Influence of Poisson's ratio ν_I for $\mu^* < 0.4$, $\lambda = \mu$.

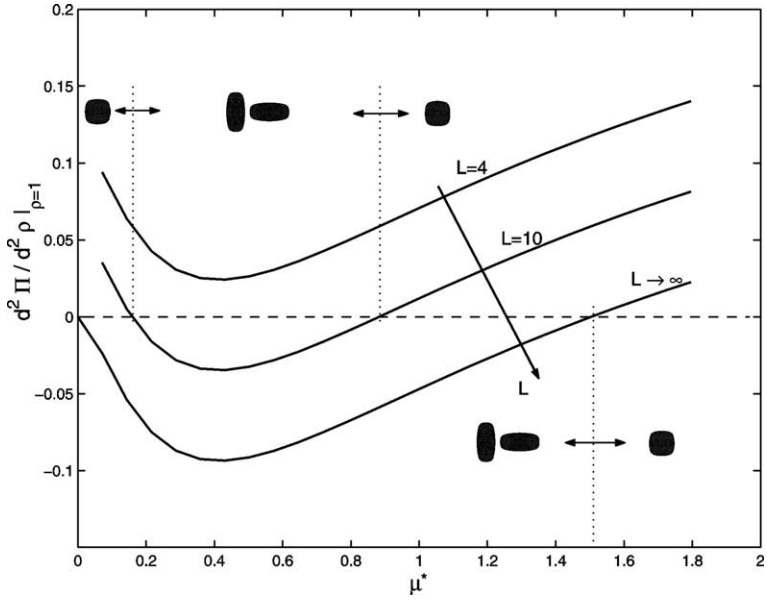

Fig. 7. Curvature for different particle sizes ($A = 2.5$).

shapes. Thus, the given explanation with respect to Fig. 3 is also valid in this anisotropic case. However, a shifting of the asymptote up to a higher value of $\mu^*_{as} \approx 1.5$ can be detected for $L \to \infty$. Thus, the asymptote μ^*_{as} redefines the names of "soft", "hard" and "homogeneous" in the common way. An anisotropic "hard" particle with $\mu^* > 1$ might have the same bifurcation behaviour as an isotropic soft particle with $\mu^* < 1$.

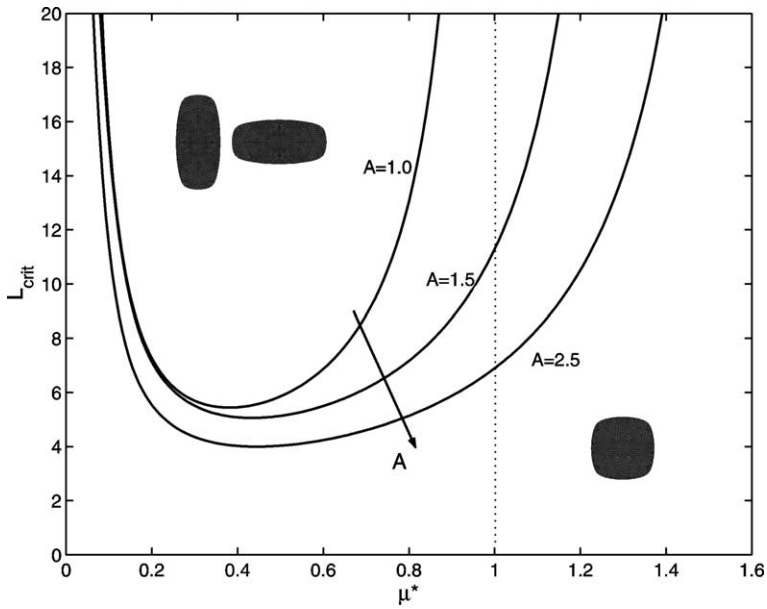

Fig. 8. Influence of the stiffness ratio μ^*.

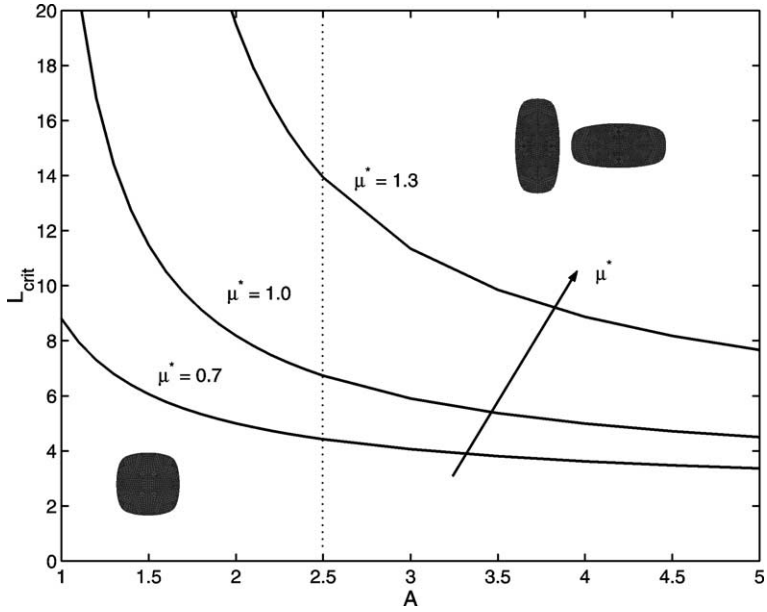

Fig. 9. Influence of the anisotropy A and μ^*.

This behaviour is also shown in detail in Fig. 8. The influence of the stiffness ratio on the bifurcation point is plotted for various anisotropy ratios. The dotted line shows the asymptote for the isotropic case. An increase of the anisotropy causes a distinct shift of the asymptote and causes a decrease of the bifurcation point at the same time. Thus, isotropy has a stabilizing effect to the equi-axed equilibrium shape.

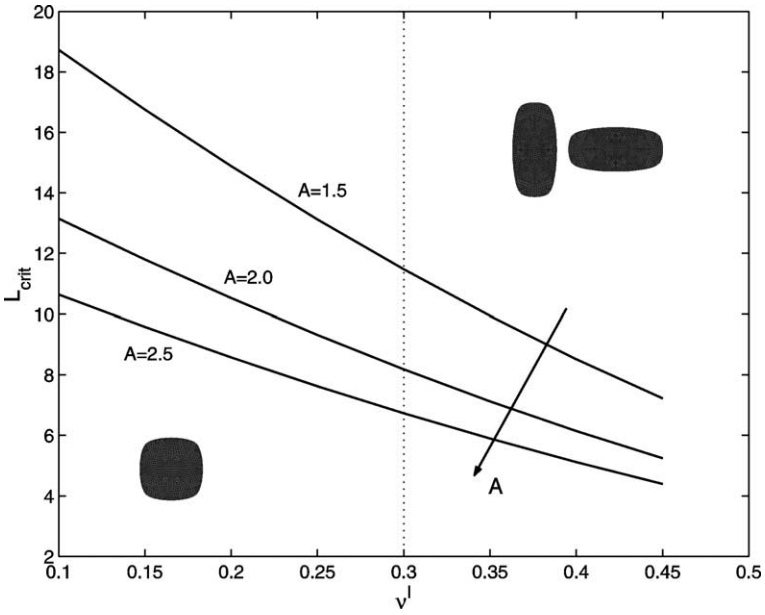

Fig. 10. Influence of ν_I and anisotropy A ($\mu^* = 1.0$).

Fig. 9 presented a graphical realisation of this statement for various stiffness ratios. The bifurcation point is a monotonous decreasing function of the anisotropy. The influence of the stiffness ratio depends on the value of μ^*. If $\hat{\mu}^*$ denotes the minimum of $L_{\text{crit}}(\mu^*)$, the stiffness ratio stabilizes the equilibrium shape for $\mu^* < \hat{\mu}^* \vee \mu^* > \hat{\mu}^*$. Within this picture, the stabilizing effect for $\mu^* > \hat{\mu}^*$ is shown.

The effect of the inner Poisson ratio is depicted in Fig. 10. Like in the isotropic case, $L_{\text{crit}}(\nu_I)$ is a monotonous decreasing function. A decrease of ν_I stabilizes the equilibrium shape. The higher the value of the anisotropy A the earlier the bifurcation starts. Again, isotropy stabilizes the system. Further investigations have shown that the influence of the stiffness ratio is comparable to the isotropic case.

However, it should be mentioned at this point that all the discussed parameters also have an influence on the "circular character" of the equilibrium shape: in the anisotropic case, the increase of the particle size results in a more and more cube like shape, which is well known by Ostwald-ripening during particle growth. This further effect has been discussed in detail by Schmidt and Gross (1997) and Mueller and Gross (1998).

4.2. Some macroscopical aspects

The change in the microstructure due to the particle morphology results in a change of the overall properties in two phase materials. Some tendencies of this macroscopical response are given in the following examples. For this purpose, the isotropic reference configuration $A = 1$ with the parameters $\lambda = \mu$, the stiffness ratio $\mu^* = 0.5$ and the particle size $L = 8.5$ is considered. This choice leads to an unstable equilibrium shape of $\rho^*_{\text{equ}} = 0$ and two stable elongated shapes of about $\rho^*_{\text{equ}} = \pm 0.3$ in the case of an infinite matrix domain ($c := c_I \to 0$). For the numerical treatment of higher volume fractions, the boundary conditions corresponding to Eq. (11) are used. Because of the fact of isotropy, the FEM-results can be compared to the analytical approximations of Voigt and Reuss (14), dilute distribution (15) and Mori–Tanaka (16).

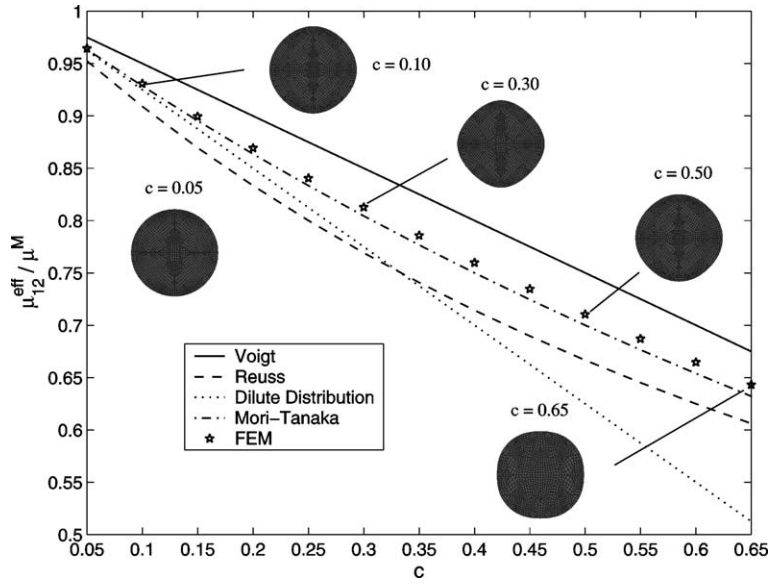

Fig. 11. Effective shear modulus ($A = 1.0$, $\rho^*_{equ} = 0$, $L = 8.5$).

The evaluation of (13) for $\rho^*_{equ} = 0$ yields an effective stiffness tensor $\mathbb{C}^{eff}$, which is isotropic due to the introduced approximations. The effective shear component μ_{12}^{eff} is depicted in Fig. 11 in dependence of the volume faction c. The effective shear modulus decreases for a higher volume fraction of the softer phase. The solid line presents the upper bound of the Voigt approximation, the dashed line the lower bound by Reuss. The equilibrium shape of the inclusion depends strongly on the volume fraction c. This dependency is also shown in the figure. For a small volume fraction, the inclusion has almost an ideal circular shape. For higher values of c, the equilibrium shape becomes more and more cuboidal in [1 1 0]-direction ($c = 0.30$), then circular again ($c = 0.50$) and finally cuboidal in [1 0 0]-direction. This yields an anisotropic effective stiffness tensor (see Fig. 12). For a discussion of the role of the volume fraction due to the stability of the equilibrium shape, see (Schmidt and Gross, 1997; Mueller et al., 2000). Although not a purely circular shape of the isotropic particle, the FEM-results are in good agreement with the approximation of Mori–Tanaka. The dilute distribution, of course, is only valid for a small volume fraction, deviates more and more from the numerical result for increasing c and is not valid for $c > 0.25$.

The evaluation of $\mathbb{C}^{eff}$ for $\rho^*_{equ} \neq 0$ leads always to an effective orthotropic stiffness tensor. The qualitative behaviour of the curve for μ_{12}^{eff} is comparable to Fig. 11. A more interesting effect is the effective anisotropy of the overall properties induced by elliptical inclusions. Fig. 12 shows the dependency of the effective anisotropy on the volume fraction for the considered particle size. Even for a small volume fraction $c = 0.1$, the macroscopical anisotropy of the composite decreases of about 2% for the equilibrium shapes elongated in [1 0 0]-direction and increases of about 1% for the shapes elongated in [0 1 0]-direction. This effect is getting more and more significant for a higher volume fraction. The equilibrium shapes of the elongated particles vary hardly from the ideal ellipsoidal shape.

Finally, the influence of the particle elongation due to the macroscopical response is discussed. Fig. 13 shows the effective shear modulus in dependence of the aspect ratio ρ^* for a volume fraction of $c = 0.10$. Again, the numerical results are in a good agreement with the approximations by Mori and Tanaka. The effective stiffness decreases for elliptical inclusions, i.e. independent of the direction of elongation. The material reaches its maximum stiffness for circular shapes. The same results are obtained by the investi-

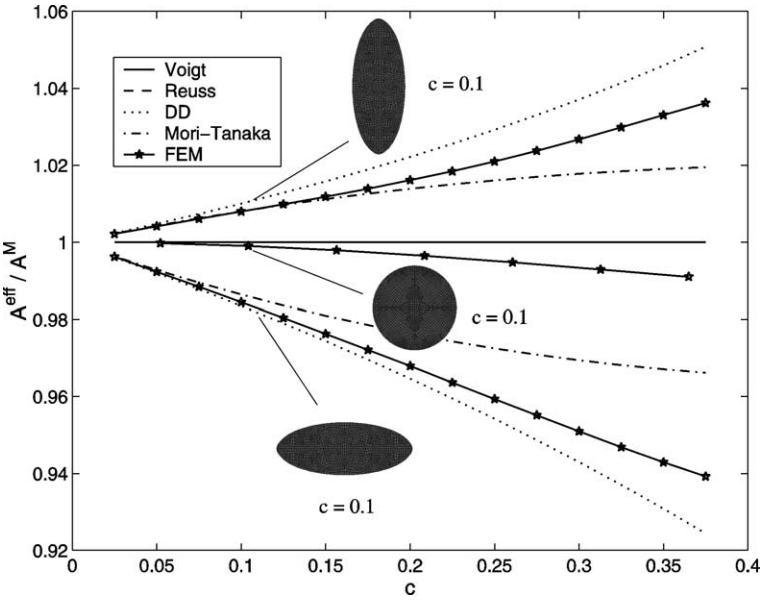

Fig. 12. Macroscopical anisotropy for $L = 8.5$.

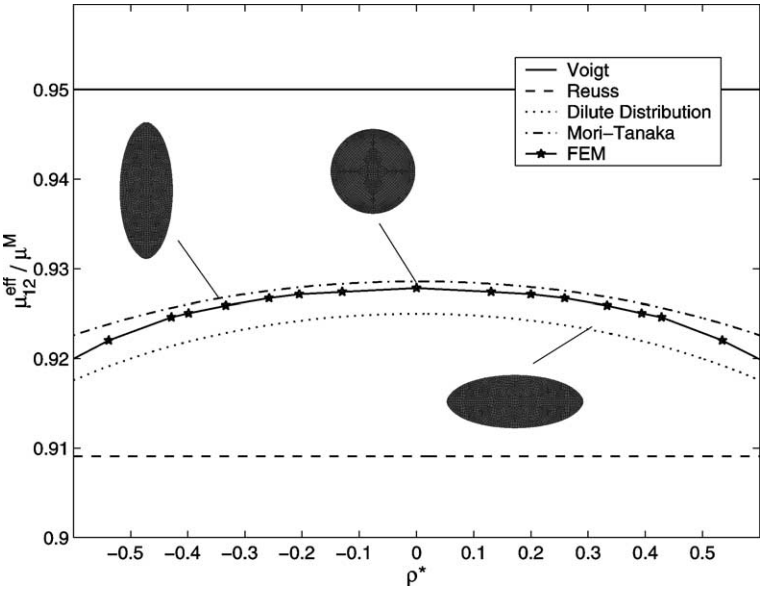

Fig. 13. Effective shear modulus for various particle sizes.

gations of orthotropic particles, where the cuboidal shapes increases the overall stiffness of the material. This behaviour can be observed by rafting experiments, where a decrease in the overall stiffness is detectable associated with a directional elongation of the particles (Wahi, 1997). The results on stabilization of the particle shape are also relevant for the design of the overall material properties.

5. Conclusions

A numerical investigation of the stability of equilibrium shapes of coherent precipitates has been presented. Elastically inhomogeneous, misfitting particles with dilatational eigenstrain have been considered. A variational principle for an elastic inclusion has been used to derive a necessary (but not sufficient) condition for an equilibrium shape. It was shown that the elastic constants, particle size and inhomogeneity are relevant factors for the stability of an equilibrium shape. For the macroscopical response, the volume fraction of the particles has been additionally taken into account. For the numerical treatment, the field equations and the configurational forces have been solved by the finite element method. The effective overall properties of the composite have been determined simply by the quantities on the cell boundary. The necessary modifications for stabilizing the equi-axed morphologies have been pointed out.

Appendix A. Discretization of the interface

Elastic part. First, we derive the relation between the discrete configurational force acting on the finite element node $\mathbf{G}^I$ in (19) and the configurational force G_n per unit area in (9). Both are results of the variational principle due to the total potential Π with respect to a virtual movement of a point (or node) $\boldsymbol{x}^I$ on the interface:

$$\delta\Pi = \mathbf{G}^I \cdot \delta\boldsymbol{x}^I = -\int_{\partial\Omega_s} \mathsf{G}_\mathrm{n}^\mathrm{el}\,\delta n\,\mathrm{d}s. \tag{A.1}$$

Here $\partial\Omega_s$ is the element boundary along the interface $\partial\mathscr{B}$. To obtain the discrete values due to δn, we chose linear shape functions $N^I(s)$ for the interface (see Fig. 14):

$$\delta n = N^I(s)\delta n^I. \tag{A.2}$$

The variation in normal direction is given by $\delta\boldsymbol{x}^I = \boldsymbol{n}\,\delta n^I$. Thus, we obtain:

$$\begin{aligned}\mathbf{G}\cdot\delta\boldsymbol{x}^I &= -\int_{\partial\Omega_s} {}^I\mathsf{G}_\mathrm{n}^\mathrm{el}\,\delta n\,\mathrm{d}s \Longleftrightarrow \underbrace{\mathbf{G}^I\cdot\boldsymbol{n}}_{=\mathbf{G}_n^\mathrm{I}}\delta n^I \\ &= -\int_{\partial\Omega_s}^{I} \mathsf{G}_\mathrm{n}^\mathrm{el} N^I(s)\delta n^I\,\mathrm{d}s \Longleftrightarrow \left[\mathbf{G}_n^I + \int_{\partial\Omega_s} {}^I\mathsf{G}_\mathrm{n}^\mathrm{el} N^I(s)\,\mathrm{d}s\right]\delta n^I = 0.\end{aligned} \tag{A.3}$$

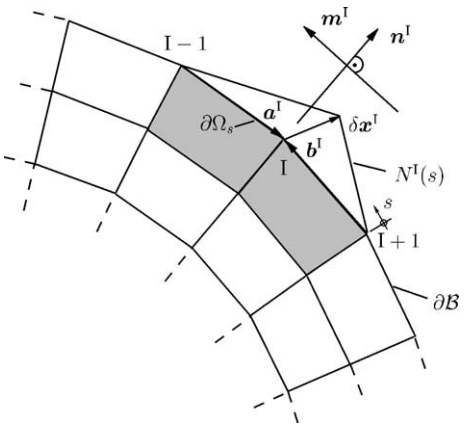

Fig. 14. Discretized interface $\partial\mathscr{B}$.

Here ${}^{I}\mathsf{G}_{\mathrm{n}}^{\mathrm{el}}$ denotes the force $\mathsf{G}_{\mathrm{n}}^{\mathrm{el}}$ acting on the node I. Since Eq. (A.3) has to be fulfilled for arbitrary δn^I, the bracket has to vanish. This leads to the required relationship:

$$\mathbf{G}_n^I = -\int_{\partial\Omega_s}^{I} \mathsf{G}_{\mathrm{n}}^{\mathrm{el}} N^J(s)\,\mathrm{d}s. \tag{A.4}$$

Interface part. For calculating the configurational force ${}^{I}\mathsf{G}_{\mathrm{n}}^{\mathrm{int}}$ acting on the node I according to Eq. (9), the curvature κ^I at this node has to be known. We chose an equi-distant mesh at the interface and approximate κ^I by the curvature of a circle defined by the three nodes $I-1$, I and $I+1$. The unit vector $\boldsymbol{m}^I$ at the node I is given by

$$\boldsymbol{m}^I = \frac{\boldsymbol{x}^{I+1} - \boldsymbol{x}^{I-1}}{|\boldsymbol{x}^{I+1} - \boldsymbol{x}^{I-1}|}. \tag{A.5}$$

The normal unit vector $\boldsymbol{n}^I$ is orthogonal to $\boldsymbol{m}$: $n_x^I = m_y^I$ and $n_y^I = -m_x^I$. Now we define the vectors $\boldsymbol{a}^I = \boldsymbol{x}^I - \boldsymbol{x}^{\mathrm{I}-1}$ and $\boldsymbol{b}^I = \boldsymbol{x}^{I+1} - \boldsymbol{x}^I$, which connect the nodes $I-1$ and $I+1$ with I (see Fig. 14) and obtain the (negative) curvature to be

$$\kappa^I = -\frac{2\sin\alpha^I}{|\boldsymbol{a}^I|} \quad \text{where } \alpha^I = \arccos\left(\frac{\boldsymbol{b}^I \cdot \boldsymbol{m}^I}{|\boldsymbol{b}^I||\boldsymbol{m}^I|}\right). \tag{A.6}$$

References

Binder, K. (Ed.), 1986. Monte Carlo Methods in Statistical Physics. Springer, Berlin, Heidelberg, New York, Barcelona, Hong Kong, London, Milan, Paris, Singapore, Tokyo.

Cahn, J.W., Hilliard, J.E., 1958. Free energy of a non-uniform system. I. Interfacial free energy. J. Chem. Phys. 28 (1), 258–267.

Dreyer, W., Müller, W.H., 2000. A study of the coarsening in tin/lead solders. Int. J. Solids Struct. 37 (28), 3841–3871.

Eshelby, J.D., 1951. The force on an elastic singularity. Phil. Trans. Roy. Soc. A. (244), 87–112.

Eshelby, J.D., 1970. Energy relations and the energy-momentum tensor in continuum mechanics. In: Kanninen, 1970, pp. 77–115.

Glotzer, S.C., Stauffer, D., Naeem, J., 1994. Monte Carlo simulations of phase separation in chemically reactive binary mixtures. Phys. Rev. Lett. 72 (26), 4109–4112.

Kanninen, M.F. (Ed.), 1970. Inelastic Behaviour of Solids. McGraw-Hill, New York.

Kolling, S., Gross, D., 2001. Simulation of microstructural evolution in materials with misfitting precipitates. J. Probab. Eng. Mech. 16 (4), 313–322.

Kolling, S., Baaser, H., Gross, D., 2002. Material forces due to crack-inclusion interaction. Int. J. Fract. 118, 229–238.

Kolling, S., Mueller, R., Gross, D., 2003. A computational concept for the kinetics of defects in anisotropic materials. Computat. Mater. Sci. 26, 87–94.

Küpper, T., Masbaum, N., 1994. Simulation of particle growth and Ostwald ripening via the Cahn–Hillard equation. Acta Metall. Mater. 42 (6), 1847–1858.

Lee, J.K., 1995. Coherency strain analysis via a discrete atom method. Scripta Metall. Mater. 32 (4), 559–564.

Lee, J.K., 1996. A study on coherency strain and precipitate morphology via a discrete atom method. Metal. Mater. Trans. 27 (A), 1449–1459.

Mueller, R., Gross, D., 1998. 3D simulation of equilibrium morphologies of precipitates. Computat. Mater. Sci. 11, 35–44.

Mueller, R., Gross, D., 1999. 3D inhomogeneous misfitting second phase particles—equilibrium shapes and morphological development. Computat. Mater. Sci. 16, 53–60.

Mueller, R., Eckert, S., Gross, D., 2000. 3D equilibrium shapes of periodically arranged anisotropic precipitates with elastic misfit. Arch. Mech. 52 (4–5), 663–683.

Mueller, R., Kolling, S., Gross, D., 2002. On configurational forces in the context of the finite element method. Int. J. Numer. Meth. Eng. 53, 1557–1574.

Mura, T., 1987. Micromechanics of Defects in Solids. Martinus Nijhoff Publishers.

Nemat-Nasser, S., Hori, M., 1993. Micromechanics: Overall Properties of Heterogeneous Materials. North Holland, Amsterdam, London, New York, Tokyo.

Schmidt, I., Gross, D., 1995. A strategy for determining the equilibrium shape of an inclusion. Arch. Mech. 47, 379–390.
Schmidt, I., Gross, D., 1997. The equilibrium shape of an elastically inhomogeneous inclusion. J. Mech. Phys. Solids 45, 1521–1549.
Schmidt, I., Gross, D., 1999. Directional coarsening in Ni-base superalloys: analytical results for an elasticity-based model. Proc. R. Soc. Lond. A (455), 3085–3106.
Socrate, S., Parks, D.M., 1993. Numerical determination of the elastic driving force for directional coarsening in Ni–superalloys. Acta Metall. Mater. 41 (7), 2185–2209.
Steinmann, P., 2000. Application of Material Forces to Hyperelastostatic Fracture Mechanics. I: Continuum Mechanical Setting. Int. J. Solids Struct. 37, 7371–7391.
Steinmann, P., Ackermann, D., Barth, F.J., 2001. Application of material forces to hyperelastostatic fracture mechanics. II. Computational setting. Int. J. Solids Struct. 38, 5509–5526.
Thompson, M.E., Su, C.S., Voorhees, P.W., 1994. The equilibrium shape of a misfitting precipitate. Acta Metall. Mater. 42 (6), 2107–2122.
Wahi, R.P., 1997. Nickel base superalloys: deformation characteristics at elevated temperatures. In: Atluri, S.N., Yagawa, G. (Eds.), Advances in Computational Engineering Science. Tech Science Press, Forsyth, Georgia, USA, pp. 85–90.